Computers & Fluids 115 (2015) 115–123

Contents lists available at ScienceDirect

Computers & Fluids

journal homepage: www.elsevier.com/locate/compfluid

Implicit dual-time stepping method for a solar wind model in spherical coordinates

Man Zhang, Xueshang Feng *

SIGMA Weather Group, State Key Laboratory for Space Weather, Center for Space Science and Applied Research, Chinese Academy of Sciences, Beijing 100190, China

ARTICLE INFO

Article history:
Received 4 September 2014
Received in revised form 8 March 2015
Accepted 26 March 2015
Available online 3 April 2015

Keywords:
Implicit dual time-stepping method
Magnetohydrodynamics equations
Solar wind

ABSTRACT

In this paper, an implicit dual-time stepping scheme based on the finite volume method in spherical coordinates with a six-component grid system is developed to model the steady state solar wind. By adding a pseudo-time derivative to the magnetohydrodynamics equations for the solar wind plasma, the governing equations are solved implicitly at each physical time step by advancing in pseudo time. As a validation, ambient solar wind for Carrington rotation 2048 has been studied. Numerical tests with different Courant factors show its capability of producing structured solar wind and that the physical time step can be enlarged to be one hundred times that of the original one. Our numerical results have demonstrated overall good agreements with the observations.

© 2015 Elsevier Ltd. All rights reserved.

1. Introduction

Over the last few decades, numerical simulations of the solar wind plasma flow have evolved from a topic only addressed in basic research toward a promising tool used for space weather prediction. Today's maturation of computational magnetohydrodynamic (MHD) dynamics has enabled us to numerically capture the basic structures of the solar wind plasma flow and transient phenomena such as the solar wind background and coronal mass ejections (CMEs) [1]. Of course, besides the numerical aspect, numerical space weather modeling depends heavily on the understanding of the fundamental physics processes, such as the coronal heating/solar wind acceleration, initiation of solar eruptions like CMEs, which will benefit from further theoretical investigation, and spacecraft observation. This rapid development of numerical space weather modeling can be attributed to both the achievement of efficient solution algorithms and the continuous increase in available computational power. With today's level of maturity in numerical algorithms, it is tempting to assume that further progress in the applicability of numerical methods may be guaranteed by solely relying on the sustained development of computer technology. However, since the relevant problem size will continue to increase as fast as available hardware permits, a number of severe challenges in the development of numerical methods for solar wind plasma flow simulation remain. Globally, without going into detail, these challenges may be summarized by the terms efficiency, robustness, and accuracy, as usually met in other computational fields [2,3].

The MHD description governs the large-scale dynamics of solar wind plasmas. Mathematically, ideal MHDs form a hyperbolic partial differential equation (PDE) system, in which seven waves appear, labeled as entropy, forward and backward slow, forward and backward Alfvén, and forward and backward fast families, which all behave anisotropic. The associated seven wave speeds are the local velocity, v, and the sets are $v \pm v_{\text{Slow}}, v \pm v_{\text{Alfven}}$, $v \pm v_{\text{Fast}}$, where v_{Slow} denotes slow magnetoacoustic speeds, while v_{Fast} indicates fast. Together with the Alfvén speed, v_{Alfven}, they are ordered since $v_{\text{Slow}} \leqslant v_{\text{Alfven}} \leqslant v_{\text{Fast}}$. Currently, many solar-terrestrial physics phenomena that require the solution of a hyperbolic system of MHD equations involve vastly different physical timescales and spatial scales. With respect to efficiency in the numerical modeling of solar-terrestrial physics phenomena, one of the major breakthroughs in numerical methods for MHD simulations was the introduction of adaptive mesh refinement [4–7], and for the solution of the inviscid equations, numerical methods may now be considered as fairly effective. However, we are still frustrated by the inadequacy of today's methods to efficiently take into account the stiffness of the discrete system of equations. For a stiffness discussion in fluid dynamics, we can refer to [2,8] and references therein. For MHD equations, the same arguments hold. Discrete stiffness can generally result from distinct sources due to the use of a scalar time step, highly stretched computational meshes, and/or other physics such as dissipative/heating processes in the form of source terms. The scalar time step can fail to cope with the disparity in the propagation speeds of convective and

---

* Corresponding author.
E-mail address: fengx@spaceweather.ac.cn (X. Feng).

http://dx.doi.org/10.1016/j.compfluid.2015.03.020
0045-7930/© 2015 Elsevier Ltd. All rights reserved.

characteristic wave modes and the highly stretched computational meshes can be required for economical resolution of the spherical shell computational domain from solar corona to interplanetary space. The discrete stiffness, provoked by the highly stretched computational meshes, can be enhanced with the increase of the corresponding high cell aspect ratios by several orders of magnitude in large portions of the computational domain which results in severe convergence problems and very high computation times, particularly in solar wind simulation studies [3].

In general, the MHD equations of the solar wind plasma involve a wide separation in timescales. The slow wave and Alfvén wave only propagate in the direction parallel to the background magnetic field whereas the propagation of the fast wave is nearly isotropic [9]. Hence, the spatial resolution requirements perpendicular to the magnetic field are much more severe than those parallel to the magnetic field, making the Courant–Friedrichs–Lewy (CFL) condition associated with the fast wave much more restrictive than that associated with the others; typically by two or more orders of magnitude. Since the fast wave is the only one that compresses the magnetic field, the fast wave sets the maximum allowable time step when using an explicit time advance. It is generally believed that when the MHD equations are used to study plasma phenomena occurring on time scales as short as the transit time of a fast MHD wave, an implicit scheme removes the numerically imposed time-step constraint allowing much larger time steps [9,10]. Besides implicit time integration, the use of dual time stepping, allows, to some extent, the physical time step to not be limited by the corresponding values in the smallest cell and to be selected based on the numerical accuracy criterion [2]. The dual time step, which does not modify the original transient evolution of the governing equation, adds a pseudo-time derivative to the governing equation. It uses the pseudo-time steady-state solution to approach the physical-time solution. A dual time marching method for MHD-like equations has been used [11–15] for the simulation of MHD phenomena.

The objective of the present paper is to explore an implicit dual time-stepping method for 3D MHD studies of ambient solar wind.The paper is organized as follows. In Section 2, the governing MHD equations of the solar wind plasma in spherical coordinates are briefly provided. In Section 3, the hybrid finite volume scheme of combining the fluid part of the MHD equations and the constraint transport method for the magnetic induction part with dual time stepping are described. In Section 4, the numerical results of ambient solar wind for Carrington rotation (CR) 2048 with different CFL numbers or Courant factors are presented. Finally, conclusions are made.

2. Governing equations

The magnetic field, $\mathbf{B} = \mathbf{B}_1 + \mathbf{B}_0$, is split into the sum of a time-independent potential magnetic field, B_0, and a time-dependent deviation, B_1 [16,17]. Here, $\mathbf{B}_0$ is a potential magnetic field, and in the present paper it is taken as the initial value with $\frac{\partial \mathbf{B}_0}{\partial t} = 0, \nabla \cdot \mathbf{B}_0 = 0, \nabla \times \mathbf{B}_0 = 0$. We note that MHD equations can be viewed as a combination of fluid dynamics coupled with magnetic fields. In the present paper, this physical splitting of the MHD equations into fluid and magnetic parts [18,19] is considered in order to design efficient finite volume (FV) schemes with spatial discretization for the fluid equations and the magnetic induction equation adopted from [20]. The fluid part of the vector, $\mathbf{U} = (\rho, \rho v_r, \rho v_\theta, \rho v_\phi r \sin\theta, e)^T$, reads as follows:

$$\frac{\partial \mathbf{U}}{\partial t} + \frac{1}{r^2}\frac{\partial}{\partial r} r^2 \mathbf{F} + \frac{1}{r\sin\theta}\frac{\partial}{\partial \theta}\sin\theta \mathbf{G} + \frac{1}{r\sin\theta}\frac{\partial}{\partial \phi}\mathbf{H} = \mathbf{S} \tag{1}$$

$$\mathbf{F} = \begin{pmatrix} \rho v_r \\ \rho v_r^2 + p + \frac{-B_{1r}^2 + B_{1\theta}^2 + B_{1\phi}^2}{2\mu} + \frac{-B_{1r}B_{0r} + B_{1\theta}B_{0\theta} + B_{1\phi}B_{0\phi}}{\mu} \\ \rho v_r v_\theta - \frac{B_{1r}B_{1\theta} + B_{1r}B_{0\theta} + B_{0r}B_{1\theta}}{\mu} \\ \left(\rho v_r v_\phi - \frac{B_{1r}B_{1\phi} + B_{1r}B_{0\phi} + B_{0r}B_{1\phi}}{\mu}\right) r\sin\theta \\ \left(\frac{1}{2}\rho v^2 + \frac{\gamma p}{\gamma - 1}\right) v_r + \frac{B_{1\theta}}{\mu}(v_r B_\theta - v_\theta B_r) + \frac{B_{1\phi}}{\mu}(v_r B_\phi - v_\phi B_r) \end{pmatrix}$$

$$\mathbf{G} = \begin{pmatrix} \rho v_\theta \\ \rho v_r v_\theta - \frac{B_{1r}B_{1\theta} + B_{1r}B_{0\theta} + B_{0r}B_{1\theta}}{\mu} \\ \rho v_\theta^2 + p + \frac{B_{1r}^2 - B_{1\theta}^2 + B_{1\phi}^2}{2\mu} + \frac{B_{1r}B_{0r} - B_{1\theta}B_{0\theta} + B_{1\phi}B_{0\phi}}{\mu} \\ \left(\rho v_\theta v_\phi - \frac{B_{1\theta}B_{1\phi} + B_{1\theta}B_{0\phi} + B_{0\theta}B_{1\phi}}{\mu}\right) r\sin\theta \\ \left(\frac{1}{2}\rho v^2 + \frac{\gamma p}{\gamma - 1}\right) v_\theta + \frac{B_{1r}}{\mu}(v_\theta B_r - v_r B_\theta) + \frac{B_{1\phi}}{\mu}(v_\theta B_\phi - v_\phi B_\theta) \end{pmatrix}$$

$$\mathbf{H} = \begin{pmatrix} \rho v_\phi \\ \rho v_r v_\phi - \frac{B_{1r}B_{1\phi} + B_{1r}B_{0\phi} + B_{0r}B_{1\phi}}{\mu} \\ \rho v_\theta v_\phi - \frac{B_{1\theta}B_{1\phi} + B_{1\theta}B_{0\phi} + B_{0\theta}B_{1\phi}}{\mu} \\ \left(\rho v_\phi^2 + p + \frac{B_{1r}^2 + B_{1\theta}^2 - B_{1\phi}^2}{2\mu} + \frac{B_{1r}B_{0r} + B_{1\theta}B_{0\theta} - B_{1\phi}B_{0\phi}}{\mu}\right) r\sin\theta \\ \left(\frac{1}{2}\rho v^2 + \frac{\gamma p}{\gamma - 1}\right) v_\phi + \frac{B_{1r}}{\mu}(v_\phi B_r - v_r B_\phi) + \frac{B_{1\theta}}{\mu}(v_\phi B_\theta - v_\theta B_\phi) \end{pmatrix}$$

where $e = \frac{1}{2}\rho \mathbf{v}^2 + \frac{p}{\gamma - 1} + \frac{1}{2}\mathbf{B}_1^2$ corresponds to the modified total energy density consisting of the kinetic, thermal, and magnetic energy densities (written in terms of $\mathbf{B_1}$). ρ is the mass density, $\mathbf{v} = (v_r, v_\theta, v_\phi)$ are the flow velocities in the frame rotating with the Sun, p is the thermal pressure, and $\mathbf{B} = \mathbf{B_0} + \mathbf{B_1}$ denotes the total magnetic field consisting of the time-independent potential magnetic field $\mathbf{B_0}$ and its time-dependent derived part, $\mathbf{B_1}$. Since $\mathbf{B_0}$ is constant with time, many terms near $\mathbf{B_0}$ on the right-hand side vanish. t and $\mathbf{r}$ are time and position vectors originating at the center of the Sun. $\mu = 4 \times 10^{-7}\pi$ is the magnetic permeability of free space, $\mathbf{g} = -\frac{GM_s}{r^3}\mathbf{r}$ is the solar gravitational force, $G = 6.673 \times 10^{-11}$ m^3 s^{-2} kg^{-1} is the gravitational constant, $M_s = 1.99 \times 10^{30}$ kg is the solar mass, and $|\Omega| = 2\pi/26.3$ rad day^{-1} is the solar angular speed. In our code, we allow the ratio of specific heats, γ, to vary from 1.05 to 1.5 along the heliocentric distance, r, according to [17], that is, $\gamma = 1.05$ for $r/R_s \leqslant 5, \gamma = 1.05 + 0.03(r/R_s - 5)$ for $5 < r/R_s \leqslant 20$, and $\gamma = 1.5$ for $r/R_s > 20$.

The source terms, $\mathbf{S} = (S_1, S_2, S_3, S_4, S_5)^T$, are generated from the polar geometrical factors, the Coriolis, centrifugal, and gravity forces, and volumetric heating source terms. Explicitly,

$$\mathbf{S} = \begin{pmatrix} 0 \\ \rho\frac{v_\theta^2 + v_\phi^2}{r} + \frac{2p}{r} + \frac{B_{1r}^2 + 2B_{1r}B_{0r}}{r\mu} - \rho\frac{GM_s}{r^2} + \rho\Omega\sin\theta(2v_\phi + \Omega r\sin\theta) + S_M \\ S_{3,1} + \rho\Omega\cos(2v_\phi + \Omega r\sin\theta) \\ -2\rho\Omega(v_\theta\cos\theta + v_r\sin\theta)r\sin\theta \\ \rho v_r\left(-\frac{GM_s}{r^2} + \Omega^2 r\sin^2\theta\right) + \rho v_\theta\Omega^2 r\sin\theta\cos\theta + S_E + v_r S_M \end{pmatrix}$$

where

$$S_{3,1} = \left(p + \rho v_\phi^2 + \frac{B_{1r}^2 + 2B_{1r}B_{0r} + B_{1\theta}^2 + 2B_{1\theta}B_{0\theta} - B_{1\phi}^2 - 2B_{1\phi}B_{0\phi}}{2\mu}\right)\frac{\cot\theta}{r} + \frac{1}{r}\left(\frac{B_{1\theta}B_{1r} + B_{1\theta}B_{0r} + B_{0\theta}B_{1r}}{\mu} - \rho v_r v_\theta\right)$$

Here, S_M and S_E stand for the momentum and energy source terms, which are responsible for the coronal heating and solar wind acceleration. Following [17], the source terms S_M and S_E are given as follows:

$$S_M = M\left(\frac{r}{R_s} - 1\right)\exp\left(-\frac{r}{L_M}\right)$$

$$S_E = Q_1 \exp\left(-\frac{r}{L_{Q_1}}\right) + Q_2\left(\frac{r}{R_s} - 1\right)\exp\left(-\frac{r}{L_{Q_2}}\right)$$

where $Q_2 = Q_0 C_a, M = M_0 C_a$, and $C_a = C'_a / max(C'_a)$ with $C'_a = \frac{(5.8-1.6e^{[1-(\theta_b/8.5)^3]})^{3.5}}{(1+f_s)^{2/7}}$. M_0, Q_0, and Q_1 in this paper are given as $7.9\times10^{-14}\,\mathrm{Nm^{-3}}$, $1.18\times10^{-7}\,\mathrm{Jm^{-3}\,s^{-1}}$, and $1.5\times10^{-9}\,\mathrm{Jm^{-3}\,s^{-1}}$, respectively. L_{Q_1}, L_{Q_2}, and L_M are set to be 1 R_s, and f_s is the magnetic expansion factor which reads $f_s = (\frac{1}{R})^2 \frac{B_{R_s}}{B_R}$, where B_{R_s} and B_R are the magnetic field strength at the solar surface and at the heliocentric distance $R = 2.5\ R_s$. θ_b is the minimum angular separation between an open magnetic field foot point and its nearest coronal hole boundary. These momentum and energy source terms are motivated by the Wang–Sheeley–Arge (WSA) model [21–23]. In writing the governing MHD equations in spherical coordinates, the geometrical curvature in spherical coordinates will turn out to produce new terms in the momentum equations, whose discretization must be accounted for and is discussed by [24]. Here, we replace the momentum equation, ρv_ϕ, with the angular momentum equation, $\rho v_\phi r \sin\theta$, [24,25] such that the geometrical curvature source term can be simplified for the ϕ-momentum.

The subsystem for the magnetic induction part runs as follows:

$$\frac{\partial B_{1r}}{\partial t} + \frac{1}{r\sin\theta}\frac{\partial}{\partial\theta}(\sin\theta(v_\theta B_r - v_r B_\theta)) - \frac{1}{r\sin\theta}\frac{\partial}{\partial\phi}(v_r B_\phi - v_\phi B_r) = 0 \quad (2)$$

$$\frac{\partial B_{1\theta}}{\partial t} - \frac{1}{r}\frac{\partial}{\partial r}(r(v_\theta B_r - v_r B_\theta)) + \frac{1}{r\sin\theta}\frac{\partial}{\partial\phi}(v_\phi B_\theta - v_\theta B_\phi) = 0 \quad (3)$$

$$\frac{\partial B_{1\phi}}{\partial t} + \frac{1}{r}\frac{\partial}{\partial r}(r(v_r B_\phi - v_\phi B_r)) - \frac{1}{r}\frac{\partial}{\partial\theta}(v_\phi B_\theta - v_\theta B_\phi) = 0 \quad (4)$$

As usual, $\rho, \mathbf{v}, p, \mathbf{B} = \mathbf{B}_1 + \mathbf{B}_0, r$, and t are normalized by the characteristic values $\rho_s, a_s, \rho_s a_s^2, \sqrt{\mu\rho_s a_s^2}, R_s$ and R_s/a_s, where ρ_s, and a_s are the density and sound speed at the solar surface.

The grid cell partition follows from the concept of a six-component grid [7,17,24,26]. That is, the spherical shell computational domain is divided into six identical component meshes to envelope a spherical surface with a partial overlap on their boundaries (Fig. 1), with each component grid defined in the spherical coordinates by

$$\left(\frac{\pi}{4} - \delta \leqslant \theta \leqslant \frac{3\pi}{4} + \delta\right) \cap \left(\frac{3\pi}{4} - \delta \leqslant \phi \leqslant \frac{5\pi}{4} + \delta\right) \quad (5)$$

where δ is proportionally dependent on the grid spacing entailed for the minimum overlapping area and is taken to be $2\Delta\theta$. Each component is confined to the same region as that in Eq. (5), but in different spherical coordinates. Vectors can be transformed from each of the six components to another [7,17,24,26]. The sliding cells, (i,j,k), are given by $[r_{im}, r_{ip}] \times [\theta_{jm}, \theta_{jp}] \times [\phi_{km}, \phi_{kp}]$ with spacings of $\Delta r(i) = r_{ip} - r_{im}, \Delta\theta(j) = \theta_{jp} - \theta_{jm}$, and $\Delta\phi(k) = \phi_{kp} - \phi_{km}$. Corresponding half-way indices defined by $im = i - 1/2(jm = j - 1/2, km = k - 1/2)$ and $ip = i + 1/2(jp = j + 1/2, kp = k + 1/2)$ mark the bounding faces of the cell, (i,j,k), where $i = 1, \ldots, N_r$, $j = 1, \ldots, N_\theta, k = 1, \ldots, N_\phi$. The grid mesh is generated as follows: $r_{im} = r_{(i-1)p}, r_{ip} = r_{im} + \Delta r(i)$, $\theta_{jm} = \theta_{(j-1)p}, \theta_{jp} = \theta_{jm} + \Delta\theta(j), \phi_{km} = \phi_{(k-1)p}, \phi_{kp} = \phi_{km} + \Delta\phi(k)$ with $r_{1m} = 1R_S, \theta_{1m} = \frac{\pi}{4}$, and $\phi_{1m} = \frac{3\pi}{4}$. The geometrical center of a cell, i,j,k, is denoted by (r_i, θ_j, ϕ_k) with $r_i = \frac{r_{im}+r_{ip}}{2}, \theta_j = \frac{\theta_{jm}+\theta_{jp}}{2}$, and $\phi_k = \frac{\phi_{km}+\phi_{kp}}{2}$. The volume-averaged coordinates $(\overline{r}_i, \overline{\theta}_j, \phi_k)$ of a cell, i,j,k, are $\overline{r}_i = \frac{3r_{ip}^4 - 3r_{im}^4}{4r_{ip}^3 - 4r_{im}^3}$, $\overline{\theta}_j = \frac{\sin\theta_{jp} - \sin\theta_{jm} - (\theta_{jp}\cos\theta_{jp} - \theta_{jm}\cos\theta_{jm})}{\cos\theta_{jm} - \cos\theta_{jp}}$. The coordinates of six face centers of a cell, i,j,k, are denoted as $(r_{im}, \theta_j^r, \phi_k), (r_{ip}, \theta_j^r, \phi_k)$, $(r_i^\theta, \theta_{jm}, \phi_k), (r_i^\theta, \theta_{jp}, \phi_k), (r_i^\phi, \theta_j^\phi, \phi_{km}), (r_i^\phi, \theta_j^\phi, \phi_{kp})$ with $r_i^\theta = r_i^\phi = \frac{2r_{ip}^3 - 2r_{im}^3}{3r_{ip}^2 - 3r_{im}^2}$, $\theta_j^r = \overline{\theta}_j, \theta_j^\phi = \frac{\theta_{jp}+\theta_{jm}}{2}$.

In order to mitigate this discrete or geometrical stiffness caused by disparate mesh cell widths, the following grid partitions are employed. For 1–25 R_s, $N_\theta = N_\phi = 42, \Delta r(i) = 0.01\ R_s$ if $r(i) < 1.1\ R_s$; $\Delta r(i) = \min(A \times \log_{10}(r(i-1)), \Delta\theta \times r(i-1))$ with $A = 0.01/\log_{10}(1.09)$ if $r(i) < 3.5\ R_s$; $\Delta r(i) = \Delta\theta \times r(i-1)$ if $r(i) > 3.5\ R_s$. In the present work, the parallel implementation in the whole computational domain of our simulated region from 1 R_s to 25 R_s is realized by a domain decomposition of six-component grids based on the spherical surface and radial direction partition.

Within the six-component grid frame, we have two boundaries: one is the inner boundary located at the solar surface, 1 R_s, and the other is the outer boundary at 25 R_s. The inner boundary at 1 R_s is fixed for simplicity. Since the outer boundary in interplanetary is a supersonic/super-Alfvénic region, the solar wind parameters at the outer boundary are set equal to the values at their nearest grid points in the computational domain. In the six-component grid system, a horizontal boundary in the (θ, ϕ) directions exists at borders in the overlapping parts, and the horizontal boundary or internal border values of each component grid are determined by interpolation from the neighbor stencils lying in its neighboring component grid. The interpolation coefficients are derived by the corresponding position of the boundary point in the stencils [17,26], the second-order Lagrange polynomial interpolation is used for the fluid flow, and the second-order reconstruction is used for the magnetic field.

As for the initial values, the magnetic field using the line-of-sight photospheric magnetic data from the Wilcox Solar Observatory is specified [17,24] to produce a 3D global magnetic field in the computational domain with the potential field source surface (PFSS) model. The initial distributions of the plasma density, ρ, pressure, p, and velocity, $\mathbf{v}$, are given by [27]. The temperature and number density on the solar surface are $T_s = 1.3 \times 10^6$ K, and $\rho_s = 1.5 \times 10^8 \mathrm{cm}^{-3}$.

3. Numerical integration formulation

Following [18,19], we designed an FV scheme for the governing equations by splitting these equations into a fluid part (Eq. (1)) and

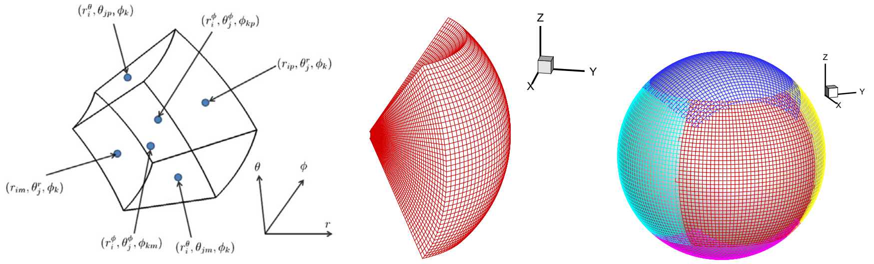

Fig. 1. Grid cell geometry with six faces located at $r = r_{im}, r = r_{ip}, \theta = \theta_{jm}, \theta = \theta_{jp}, \phi = \phi_{km}, \phi = \phi_{kp}$, and the cell center at the point $(\overline{r}_i, \overline{\theta}_j, \phi_k)$ (*left*). The partition of a sphere into six identical components with partial overlap (*middle*) and one-component mesh stacked in the r direction (*right*).

a magnetic induction part (Eqs. (2)–(4)). The fluid part leads to an extended Euler system with magnetic forces as source terms. For spatial discretization of our numerical scheme formulation, we strictly follow those of [20] by using the FV discretization of Eq. (1), and by averaging Eqs. (2)–(4) over facial areas to obtain the semi-integral forms of the magnetic induction equations. We used a semi-discrete Godunov-type central scheme for the Euler subsystem. We adopt a second-order accurate linear ansatz reconstruction [20] for the fluid part, and in the linear reconstruction the derivative terms at volume-averaged coordinates are approximated by using a minmod limiter for oscillation control. The magnetic induction equations are solved using the CT method. For consistency, the reconstruction of the magnetic induction part is also of second-order accuracy and cross derivative terms are slope-limited approximations of the exact derivatives at the cell face centers obtained using a minmod limiter. For details, refer to [20,24].

The full system is integrated over time with a second-order implicit Runge–Kutta scheme. Following the idea of [18,19], we simultaneously or sequentially integrate the MHD equations in time for the fluid part and the magnetic induction part. That is, in order to obtain a scheme for the full MHD equations, we move the discretized fluxes to the right-hand sides of Eqs. (1)–(4), and denote them by their corresponding source terms as $\mathcal{R}_{\mathbf{U}}[\overline{\mathbf{U}}, \overline{\mathbf{B}}]$ and $\mathcal{R}_{\mathbf{B}}[\overline{\mathbf{U}}, \overline{\mathbf{B}}]$, respectively, and we can advance using the following procedure:

$$\overline{\mathbf{U}}^{*} = \overline{\mathbf{U}}^{n} + \Delta t \mathcal{R}_{\mathbf{U}}[\overline{\mathbf{U}}^{*}, \overline{\mathbf{B}}^{n}] \tag{6}$$

$$\overline{\mathbf{B}}^{*} = \overline{\mathbf{B}}^{n} + \Delta t \mathcal{R}_{\mathbf{B}}[\overline{\mathbf{U}}^{n}, \overline{\mathbf{B}}^{*}] \tag{7}$$

$$\overline{\mathbf{U}}^{**} = \overline{\mathbf{U}}^{*} + \Delta t \mathcal{R}_{\mathbf{U}}[\overline{\mathbf{U}}^{**}, \overline{\mathbf{B}}^{*}] \tag{8}$$

$$\overline{\mathbf{B}}^{**} = \overline{\mathbf{B}}^{*} + \Delta t \mathcal{R}_{\mathbf{B}}[\overline{\mathbf{U}}^{*}, \overline{\mathbf{B}}^{**}] \tag{9}$$

$$\overline{\mathbf{U}}^{n+1} = \frac{1}{2}\overline{\mathbf{U}}^{n} + \frac{1}{2}\overline{\mathbf{U}}^{**} \tag{10}$$

$$\overline{\mathbf{B}}^{n+1} = \frac{1}{2}\overline{\mathbf{B}}^{n} + \frac{1}{2}\overline{\mathbf{B}}^{**} \tag{11}$$

In a cell with a geometrical center of $(i, j, k), \overline{\mathbf{U}} = \mathbf{U}(\bar{r}_i, \bar{\theta}_j, \phi_k)$ denotes the volume average for the conservative variables, **U**, and $\overline{\mathbf{B}} = (B_r(r_{im}, \theta_j^r, \phi_k), B_\theta(r^\theta, \theta_{jm}, \phi_k), B_\phi(r^\phi, \theta_j^\phi, \phi_{km}))$, where $B_r(r_{im}, \theta_j^r, \phi_k)(B_\theta(r^\theta, \theta_{jm}, \phi_k), B_\phi(r^\phi, \theta_j^\phi, \phi_{km}))$ denotes the area average for the magnetic field, $B_r(B_\theta, B_\phi)$, in face, $r(\theta, \phi)$. As usual, the time step length is prescribed by the CFL stability condition:

$$\Delta t = \mathrm{CFL}/\max\left(\sqrt{\left(\frac{|v_r| + c_{fr}}{\Delta r}\right)^2 + \left(\frac{|v_\theta| + c_{f\theta}}{r\Delta\theta}\right)^2 + \left(\frac{|v_\phi| + c_{f\phi}}{r\sin\theta\Delta\phi}\right)^2}\right) \tag{12}$$

Here, $c_{fr}, c_{f\theta}, c_{f\phi}$ are the fast magnetosonic speeds in (r, θ, ϕ) directions, defined respectively by $c_{fr} = \frac{1}{\sqrt{2}}\sqrt{c_s^2 + c_A^2 + ((c_s^2 + c_A^2)^2 - 4c_s^2\frac{B_r^2}{\mu\rho})^{\frac{1}{2}}}$, $c_{f\theta} = \frac{1}{\sqrt{2}}\sqrt{c_s^2 + c_A^2 + ((c_s^2 + c_A^2)^2 - 4c_s^2\frac{B_\theta^2}{\mu\rho})^{\frac{1}{2}}}, c_{f\phi} = \frac{1}{\sqrt{2}}\sqrt{c_s^2 + c_A^2 + ((c_s^2 + c_A^2)^2 - 4c_s^2\frac{B_\phi^2}{\mu\rho})^{\frac{1}{2}}}$, where $c_s = \sqrt{\frac{\gamma p}{\rho}}, c_A = \sqrt{\frac{B_r^2 + B_\theta^2 + B_\phi^2}{\mu\rho}}$ are the sound and Alfvénic speeds. Next, we employ a simultaneous time integration with CFL = 0.5.

In this paper, an implicit dual time-stepping scheme is used to simulate the solar wind to improve computational efficiency. A pseudo-time derivative is introduced to the original implicit form of Eqs. (6)–(9), and we adopt a first-order backward finite difference scheme for the pseudo-time derivative. For example, Eqs. (6) and (7), become new differential equations:

$$\frac{\Delta\overline{\mathbf{U}}_{i,j,k}^{*,m}}{\Delta\tau} + \frac{\overline{\mathbf{U}}_{i,j,k}^{*,m+1} - \overline{\mathbf{U}}_{i,j,k}^{n}}{\delta t} = \mathcal{R}_{\mathbf{U}}^{m+1} \tag{13}$$

$$\frac{\Delta\overline{\mathbf{B}}_{i,j,k}^{*,m}}{\Delta\tau} + \frac{\overline{\mathbf{B}}_{i,j,k}^{*,m+1} - \overline{\mathbf{B}}_{i,j,k}^{n}}{\delta t} = \mathcal{R}_{\mathbf{B}}^{m+1} \tag{14}$$

where $\Delta\overline{\mathbf{U}}_{i,j,k}^{*,m} = \overline{\mathbf{U}}_{i,j,k}^{*,m+1} - \overline{\mathbf{U}}_{i,j,k}^{*,m}, \Delta\overline{\mathbf{B}}_{i,j,k}^{*,m} = \overline{\mathbf{B}}_{i,j,k}^{*,m+1} - \overline{\mathbf{B}}_{i,j,k}^{*,m}, n$ is the physical time level, m is the pseudo-time level (the number of sub-iterations), $\Delta\tau$ is the pseudo-time step size, and δt is the physical time step size.

In our code, we examine $\delta t = 10\Delta t, 50\Delta t, 100\Delta t$ respectively. The simulation scheme will become unstable if the pseudo-time step size, $\Delta\tau$, is larger than the physical time step size, δt [28]. In this paper, the pseudo-time step size is

$$\Delta\tau = \min\left(\frac{CFL_{sub}V_{i,j,k}}{\lambda^A + \lambda^B + \lambda^C}, \frac{2\delta t}{3}\right)$$

$CFL_{sub} = 0.3$ is the CFL number for the pseudo-time step, $\lambda^A = |v_r| + c_{fr}(\lambda^B = |v_\theta| + c_{f\theta}, \lambda^C = |v_\phi| + c_{f\phi})$ is the maximum speed in the $r(\theta, \phi)$ direction, respectively.

Using a Taylor expansion for the right hand side of Eqs. (13) and (14), we get

$$\left[\left(\frac{1}{\Delta\tau} + \frac{1}{\delta t}\right)I - \left(\frac{\partial\mathcal{R}_{\mathbf{U}}}{\partial\overline{\mathbf{U}}}\right)^m\right]\Delta\overline{\mathbf{U}}_{i,j,k}^{*,m} = \mathcal{R}_{\mathbf{U}}^m - \frac{\overline{\mathbf{U}}_{i,j,k}^{*,m} - \overline{\mathbf{U}}_{i,j,k}^{n}}{\delta t} \tag{15}$$

$$\left[\left(\frac{1}{\Delta\tau} + \frac{1}{\delta t}\right)I - \left(\frac{\partial\mathcal{R}_{\mathbf{B}}}{\partial\overline{\mathbf{B}}}\right)^m\right]\Delta\overline{\mathbf{B}}_{i,j,k}^{*,m} = \mathcal{R}_{\mathbf{B}}^m - \frac{\overline{\mathbf{B}}_{i,j,k}^{*,m} - \overline{\mathbf{B}}_{i,j,k}^{n}}{\delta t} \tag{16}$$

Initially, we use $\overline{\mathbf{U}}_{i,j,k}^{*,0} = \overline{\mathbf{U}}_{i,j,k}^{n}, \overline{\mathbf{B}}_{i,j,k}^{*,0} = \overline{\mathbf{B}}_{i,j,k}^{n}$ for computation. Eqs. (15) and (16) are solved using the unfactored line Gauss–Seidel iteration [29,30]. As pointed out by [29], the standard line Gauss relaxation is feasible among comparison of a modified point Gauss relaxation, a standard Gauss–Seidel line relaxation, and the Beam–Warming alternating direction implicit (ADI) scheme, and even more efficient than that implemented with the ADI scheme in three-dimensional flows.

This method can reach a very large pseudo-time step since no factorization error is introduced. When the pseudo-time derivative is equal to zero, the original formulation is recovered. Convergence of the pseudo-time (sub-iterations) at each physical time step is important for obtaining an accurate transient solution. However, no well-established theory exists on the number of sub-iterations or residual convergences needed to obtain a specified physical-time accuracy while minimizing the computational cost per time step. Also, it is too costly to make the sub-iteration procedure perform until convergence to machine precision [31]. In this paper, besides setting up convergence criterion, $\frac{\Delta\overline{\mathbf{U}}_{i,j,k}^{*,m}}{\Delta\tau} \leqslant 10^{-6}$, of the pseudo-time (sub-iterations), we also set the maximal sub-iterations to 15 in order to avoid infinite iterations. The physical solution at new time level is updated: $\overline{\mathbf{U}}_{i,j,k}^{*} = \overline{\mathbf{U}}_{i,j,k}^{*,m+1}$. The same can be said for the magnetic part. We can also get $\overline{\mathbf{U}}_{i,j,k}^{**}$ and $\overline{\mathbf{B}}^{**}$ using this procedure, and then find the updated $\overline{\mathbf{U}}^{n+1}$ and $\overline{\mathbf{B}}^{n+1}$.

4. Numerical results

CR 2048 in 2006 during a solar activity minimum is selected for our validation study. With the numerical method described above, our aim was to achieve 3D numerical results for the solar wind plasma and magnetic field in the solar corona, which can provide typical solar wind characteristics for a solar activity minimum.

Fig. 2 shows the steady-state MHD results of the radial speed, v_r, profiles along a heliocentric distance at $\theta = 90°$ and $\theta = 174°$ for CR 2048 with $\delta t = \Delta t, 10\Delta t, 50\Delta t$, and $100\Delta t$, where Δt is the physical time step determined by the usual stability with Eq.

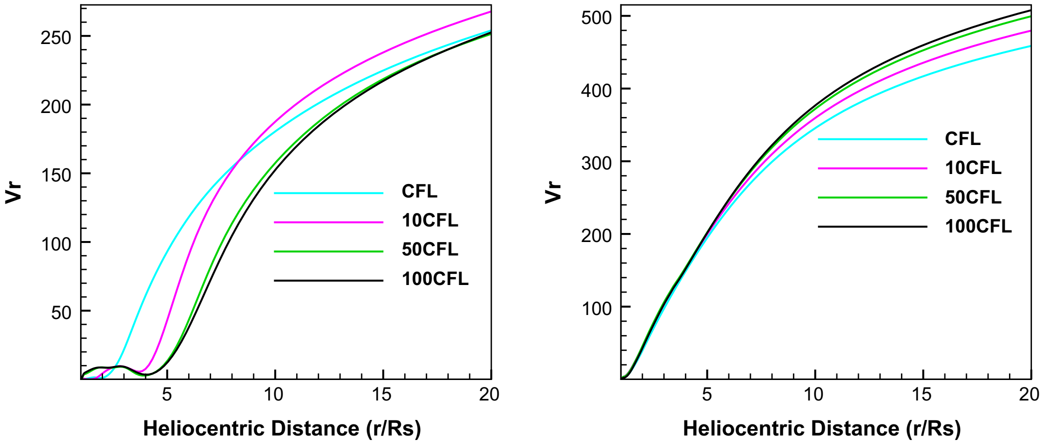

Fig. 2. The comparison of the radial speed, v_r (km/s), profiles along a heliocentric distance at $\theta = 90^\circ$ (left) and $\theta = 174^\circ$ (right) for CR 2048 with $\delta t = \Delta t, 10\Delta t, 50\Delta t$, and $100\Delta t$ at the same longitude $\phi = 0^\circ$ from 1 to 20 R_s.

(12). In this figure, $\theta = 90^\circ$ corresponds to the vicinity of the equator or the heliospheric current sheet (HCS) region (close to the equator near the solar minimum), while $\theta = 174^\circ$ corresponds to the open field region. From the model results with different δt, we can find that in the open field region the speed is larger representing the fast solar wind, while in the HCS region the speed is smaller representing the slow solar wind.

We investigated the influence of different CFL conditions on the radial speed profiles along a heliocentric distance for CFL numbers $0.5, 5.0, 25.0, 50.0$. From the numerical results of these tests, we can find the dual time stepping scheme will cause a slight oscillation of the radial speed within the inner corona around the equator (left panel of Fig. 2) without changing the general structure of the problem. As for their corresponding plots in the open field region as shown in the right panel of Fig. 2, we do not see any difference of v_r for these different CFL conditions. Overall, the scheme for different CFL works well. The slight oscillation with different CFL is caused by the history of the inflow through the solar surface, which might be slightly different in simulation with different CFL number. Also, the sub-iterations in dual time stepping scheme can cause some oscillation. If we increase the sub-iterations by setting the maximal sub-iterations up to 30 (as compared to 15 in producing Fig. 2), then the oscillation will decrease. To see this, Fig. 3 shows the radial speed and number density profiles along a heliocentric distance from 1 to 5 R_S at $\theta = 90^\circ$ for $\delta t = 100\Delta t$, in comparison with those of $\delta t = \Delta t$. We can see the oscillation become smaller compared to Fig. 2. Of course, increasing the sub-iterations will add our computational cost.

From our experiments, it is found that the convergence criterion for the pseudo-time iteration loop is significant in simulating solar wind MHD flows. In the pseudo-time iteration, using a given convergence criterion is suggested. If using a maximum iteration step, we suggest that the maximum iterations are limited in different areas along the radial direction to ensure the time accuracy and at the same time improve the computational efficiency. Similarly, near large gradient regions, increasing the pseudo-time maximum iteration and refining grid can better enhance the resolution of the numerical solution.

Next, we present our numerical results of the steady-state ambient solar wind for $\delta t = 100\Delta t$. Fig. 4 displays the radial magnetic field with a Gauss unit at 2.5 R_s for CR 2048 with $\delta t = 100\Delta t$ and PFSS. Obviously, the neutral lines from MHD and PFSS models share the same pattern.

Fig. 5 displays the number density, radial speed, and temperature maps for CR 2048 with $\delta t = 100\Delta t$ on the different surfaces at 2.5 R_s and 20 R_s. The number density decreases with the heliocentric distance while radial speed increases. The flow around the vicinity of the HCS region has a high density, low speed, and

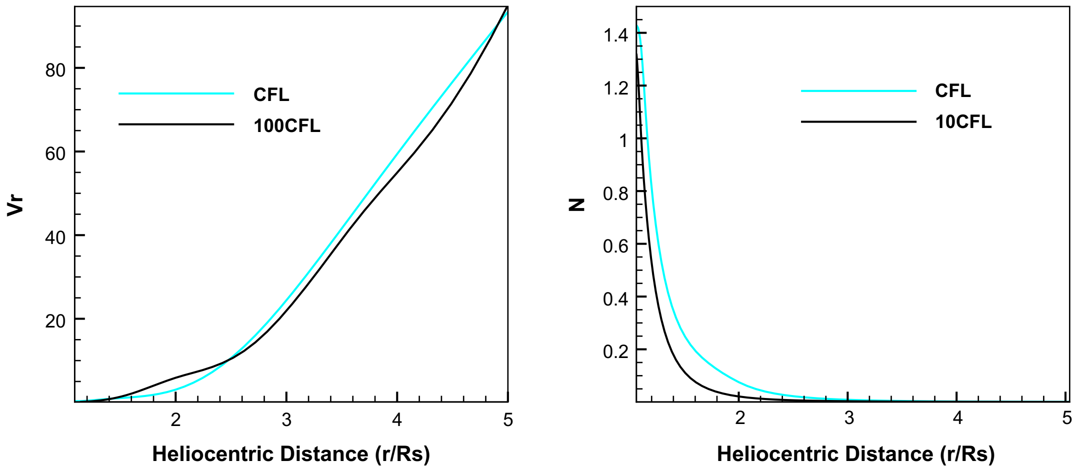

Fig. 3. The comparison of the radial speed, v_r (km/s), and number density, N (10^8 cm^{-3}), profiles along a heliocentric distance at $\theta = 90^\circ$ for CR 2048 with $\delta t = \Delta t$ and $100\Delta t$ at the same longitude $\phi = 0^\circ$ from 1 to 5 R_s.

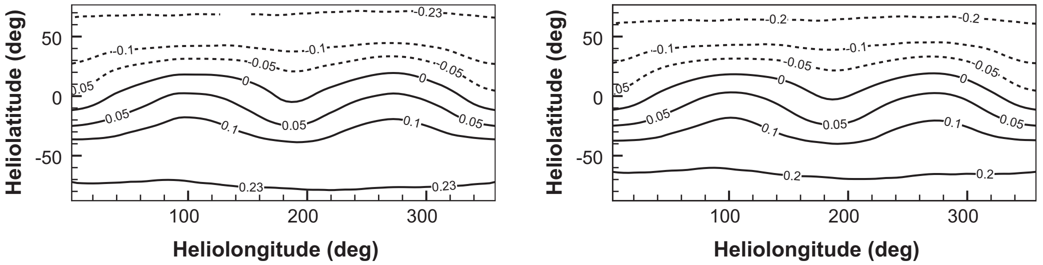

Fig. 4. The radial magnetic field with a Gauss unit at 2.5 R_s for CR 2048 with $\delta t = 100\Delta t$ (*left*) and PFSS (*right*).

low temperature, while at the polar or the open field regions the inverse condition can be seen. These structures are consistent with Fig. 7.

Fig. 6 presents the radial speed, v_r, at 5 R_s from the MHD result for CR 2048 with $\delta t = 100\Delta t$ and WSA model [21,22]. The WSA model is an empirical model that can obtain the solar wind speed in which the radial speed is defined as $v_r = 265 + \frac{1.5}{(1+f_s)^{2/7}}(5.8 - 1.6e^{[1-(\theta_b/7.5)^3]})^{3.5}$ with the use of θ_b and the expansion factor f_s [23]. f_s is the magnetic expansion factor which reads $f_s = (\frac{1}{R})^2 \frac{B_{R_s}}{B_R}$ where B_{R_s} and B_R are the magnetic field strength at the solar surface and at the heliocentric distance $R = 2.5\ R_s$. θ_b is the minimum angular separation between an open magnetic field foot point and its nearest coronal hole boundary. From this figure, we can see that the radial speed from the MHD result is smaller to that from the WSA. This is because the f_s obtained from the steady-state magnetic fields of the MHD model is bigger than that of the WSA model and will have a large expansion for the magnetic field and then present a relatively low speed. This can be interpreted physically in terms of the pressure excised by the plasma that further spreads out the magnetic field in the MHD simulation [17].

Fig. 7 shows the model results for CR 2048 with $\delta t = 100\Delta t$, the magnetic field lines, radial speed v_r, and number density N on two different meridional planes at $\phi = 180^\circ - 0^\circ$ and $\phi = 270^\circ - 90^\circ$ from 1 to 20 R_s, where the arrowheads on the black lines represent the directions of the magnetic fields. At high latitudes, the magnetic field lines extend into interplanetary space and the solar wind in this region has a faster speed and lower density. On the contrary, the slow solar wind and high density are located at lower latitudes around the HCS. We can also see a helmet streamer stretched by the solar wind in this region. Above the streamer, a thin current sheet is displayed between different magnetic polarities.

From the MHD results in Figs. 4–7 for 2.5, 5, 20 R_s, it can be seen that the density-maximum (radial speed-minimum) locations can serve as an indicator of current-sheet position, while the locations of the density-gradient maximum can be a reliable indicator of the coronal-hole boundaries. As the heliocentric distance increases from the inner corona to the outer corona, the topology of the streamer belts indeed shows a slight radial variation, gradually flattening toward the equator as the heliocentric distance increases from 2.5 to 20 R_s. This radial variation of the helmet streamer belt is governed by the inertia of the radially accelerating plasma flow.

Fig. 8 shows the model results for CR 2048 with $\delta t = 100\Delta t$, the total speed v, and a Alfvénic surface in the meridional planes of $\phi = 180^\circ - 0^\circ$ and $\phi = 270^\circ - 90^\circ$ from 1 to 20 R_s. The Alfvénic surface is indicated by the white line. The Alfvénic Mach number defined as $M_A = \frac{v\sqrt{\mu\rho}}{B}$, M_A increases from being subsonic in the inner corona (~ 0.1 or even smaller on the solar surface) to superAlfvénic in interplanetary space (~ 10 at 1 AU). Thus we have to pass the critical points $M_A = 1$ [32], where the Alfvénic critical points generate the Alfvénic surface. From Fig. 8, we can see that the Alfvénic surface is wispy, which implies that the solar wind is not spherical and higher velocities are achieved at high latitudes. In the inner corona below the Alfvénic critical points, the magnetic stress dominates the interaction. The coronal magnetic field is largely dipole-like around the minimum phase of solar activity. The gradient of the radial field strength in latitude, with stronger fields at higher magnetic latitudes, bends the stream lines from the radial direction toward the magnetic equator. However, in the corona beyond the Alfvénic critical points, it is the inertia of the radially accelerated plasma flow that dominates the magnetic field-plasma interaction. The Alfvénic critical points are not spherical-symmetrically distributed: the lowest (highest) Alfvénic critical point occurs in the equator (pole) [33,34]. The Alfvénic surface derived from the MHD results on the meridional planes roughly ranges from about 6 to 11 R_s during this CR. Possible distances for the

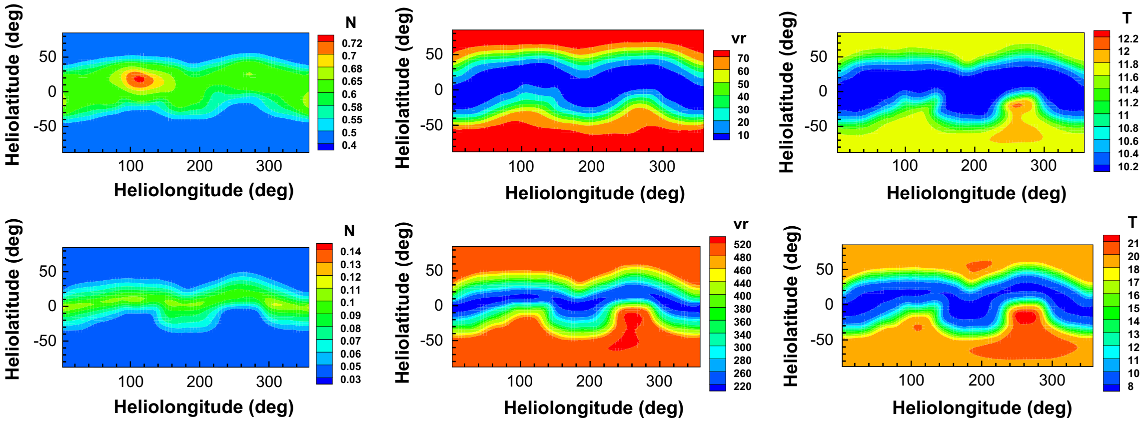

Fig. 5. The model results for CR 2048 with $\delta t = 100\Delta t$ on the different surfaces at 2.5 R_s (*top row*) and 20 R_s (*bottom row*). The left column denotes the number density, N, with units of 10^6 cm^{-3}, 10^4 cm^{-3} from top to bottom, the middle column denotes radial speed, v_r, with units of km/s, and the last column denotes temperature, T, with units of 10^5 K.

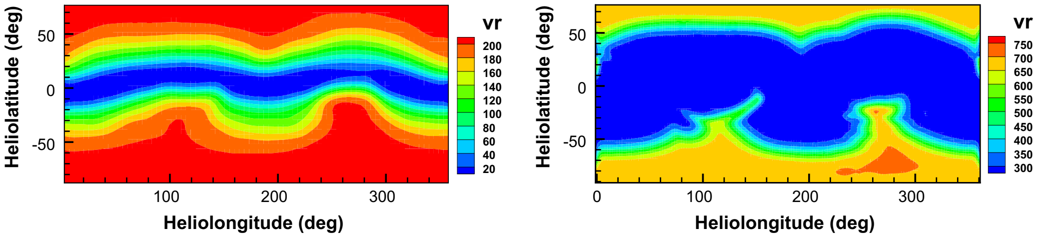

Fig. 6. The model results for CR 2048 with $\delta t = 100\Delta t$ and radial speed v_r (km/s) at 5 R_s from MHD (*left*) and WSA (*right*).

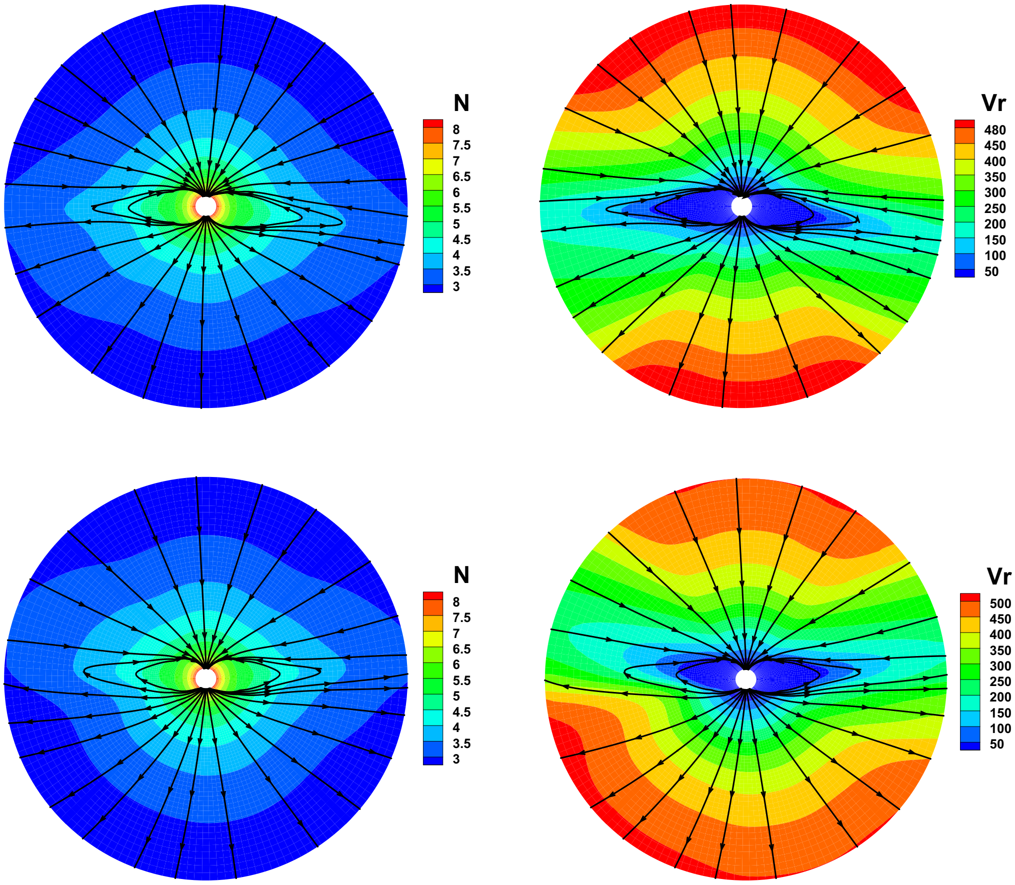

Fig. 7. The model results for CR 2048 with $\delta t = 100\Delta t$, the magnetic field lines, radial speed v_r (km/s), and number density $N(log_{10}/\mathrm{cm}^3)$ on the meridional plane of $\phi = 180^\circ - 0^\circ$ (*top*) and $\phi = 270^\circ - 90^\circ$ (*bottom*) from 1 to 20 R_s.

Alfvénic surface have been suggested by several recent works. Wang et al. [35], and Sheeley et al. [36] have observed isolated inbound retracting loops in streamers, and without observing such a feature beyond 6 R_s, they attribute this lack to a low Alfvénic surface near 6 R_s. Schwadron et al. [37] and Smith et al. [38] treat the Alfvénic surface in the context of the heliospheric flux balance, and place it at 10–15 R_s. Based on the radial evolution of the direction of the coronal magnetic field, Zhao et al. [34] showed that the coronal helmet streamer belts observed at several heights by SOHO/LASCO, together with the source surface field of the HCCSSS model [39–41], can be used to find the heliocentric distance of the lowest and highest Alfvénic critical point. The highest Alfvénic critical point around the solar minimum is located between 10 and 14 R_s. The highest radial Alfvénic critical point around the solar minimum may be located between 10 and 14 R_s, where both the effect of solar rotation can be neglected and stream-stream interactions are unimportant. Our numerical MHD results determine the location of the Alfvénic surface from 6 to 11 R_s due to the interaction of the solar wind flow and magnetic field.

In the MHD simulations, the divergence-constraint of the magnetic field is important, because the large numerical error from $\nabla \cdot \mathbf{B}$ can cause non-physical flow parallel to the magnetic field. For solar wind numerical studies, there are many discussions in the literature [e.g. 17,26,42–44]. To quantitatively see how $\nabla \cdot \mathbf{B}$ evolves, following [44], we define the relative divergence error compared to the magnetic field of the cell as follows: $\mathrm{Error}(\mathbf{B}_1, \mathbf{B}_0) = \sum_{k=1}^{M} \frac{\int_{V_k} \nabla\cdot\mathbf{B}_1 dV}{\int_{S_k} |\mathbf{B}_0| dS} / M$, $\mathrm{Error}(\mathbf{B}, \mathbf{B}_0) = \sum_{k=1}^{M} \frac{\int_{V_k} \nabla\cdot\mathbf{B} dV}{\int_{S_k} |\mathbf{B}_0| dS} / M$, $\mathrm{Error}(\mathbf{B}) = \sum_{k=1}^{M} \frac{\int_{V_k} \nabla\cdot\mathbf{B} dV}{\int_{S_k} |\mathbf{B}| dS} / M$ where M is the total number of cells in the computational domain, V_k is the kth sliding volume cell involved with the mesh grids, and S_k is the surface areas involved with V_k. $\mathrm{Error}(\mathbf{B}_1, \mathbf{B}_0)$ and $\mathrm{Error}(\mathbf{B}, \mathbf{B}_0)$ can be seen as the magnitudes of $\nabla \cdot \mathbf{B}_1$ and $\nabla \cdot \mathbf{B}$ compared relatively to the magnetic field $\mathbf{B}_0$. Fig. 9 gives the evolution of the average relative divergence error as a function of time for $\mathrm{Error}(\mathbf{B}_1, \mathbf{B}_0)$, $\mathrm{Error}(\mathbf{B}, \mathbf{B}_0)$, and $\mathrm{Error}(\mathbf{B})$. From this figure we can see that $\mathrm{Error}(\mathbf{B}_1, \mathbf{B}_0)$ is around

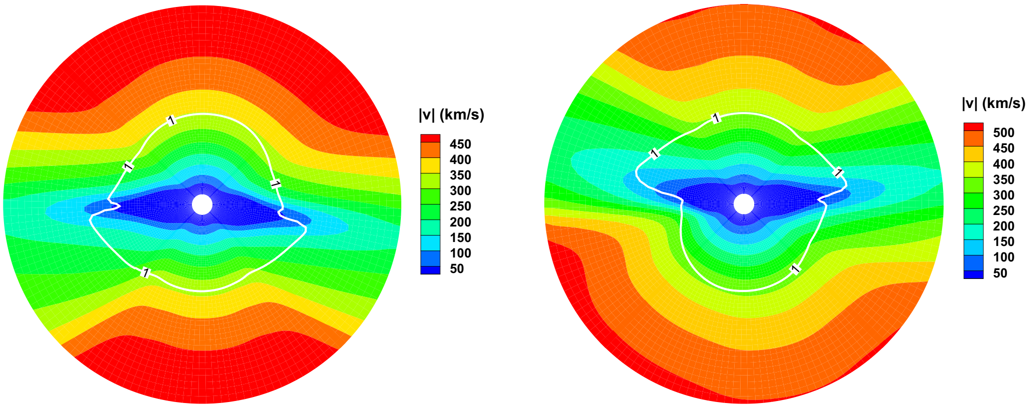

Fig. 8. The model results for CR 2048 with $\delta t = 100\Delta t$, the total speed v (km/s), and Alfvénic surface (*white line*) on the meridional plane of $\phi = 180^\circ - 0^\circ$ (*left*) and $\phi = 270^\circ - 90^\circ$ (*right*) from 1 to 20 R_s.

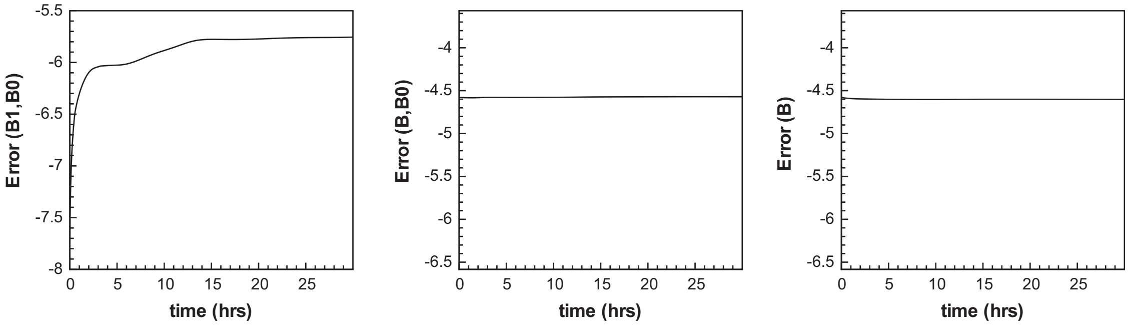

Fig. 9. The model results of temporal evolution of the log_{10} error for CR 2048 with $\delta t = 100\Delta t$.

10^{-6} and stays the same after 7 h without any obvious large error after a long run time. However, Error($\mathbf{B}$, $\mathbf{B}_0$), and Error($\mathbf{B}$) remain around $10^{-4.6}$ in the calculation, which means that $\nabla \cdot \mathbf{B}_0$ contributes much largely to $\nabla \cdot \mathbf{B}$, and that $\nabla \cdot \mathbf{B}_1$ is kept at very small level by applying CT method. This verifies that the dual-time stepping produces competitive results in successfully keeping the divergence error small. Numerical validation for solar wind simulation in this paper also suggests that non-zero errors in the field divergence do not introduce changes in the large-scale dynamics of the magnetic field. As usual, large (unresolved) gradients in the local magnetic field cause large divergence errors, and with higher resolution, the gradients are resolved better and the divergence errors become smaller.

5. Conclusions

For an ambient solar wind study, we proposed a dual time stepping method with a splitting scheme with a combing FV scheme for the fluid part in MHD equations and the constrained transport method for the magnetic induction part. This newly established scheme can avoid the complex eigenstructure of the Jacobian matrices. Implicit time integration with pseudotime stepping is used to relax the physical time step.

By adding a pseudo-time derivative to the MHD equations for the solar wind plasma, the physical time layer tracks the physical variety of the flow and the pseudo-time layer iterates to a steady-state in each physical time step. Then the physical time step is not limited by the numerical stability, while it is still based on the numerical accuracy criterion. Thus, the physical time step can be very large.

The numerical results for CR 2048 with different CFL conditions show the capability of producing structured solar wind. As an independently developed 3D MHD code, the present scheme and dual time technique has demonstrated accuracy and robustness through numerical experiments of ambient solar wind for CR 2048. Our numerical results have demonstrated overall good agreement with the observations.

The use of dual time stepping is beneficial in the computation since the physical time step is not limited by the corresponding values in the smallest cell and it is selected based on the numerical accuracy criterion.

The present dual time scheme may be able to extend the limitation of the plasma beta in the strong magnetic field region, such as solar coronal magnetic field MHD reconstruction, because of the new enlarged CFL condition.

The pseudo time iteration steps required for convergence depend on the CFL number and the grid numbers. For each physical time step, δt, it takes about 10 pseudo time iterations to meet the 10^{-6} tolerance, compared to the CFL number 0.5 without the dual-time technique it takes 100 iterations under the enlarged CFL number 50.0. Here, we only see how much the CFL number can be enlarged, without caring much about the computational time. Nonlinear iteration methods should be further investigated. Some advanced nonlinear MHD solvers [9,45–49] are at hand. Research in the area of nonlinear multigrid is essentially unexplored for extended MHD describing the solar wind plasma. Another interesting challenge in developing implicit methods for MHD is the combination of Jacobian-Free Newton–Krylov or nonlinear multigrid (also known as full approximation scheme) methods with adaptive mesh refinement (AMR).

With pseudo-time, additional acceleration techniques such as multigrid [2] and preconditioned Harten–Lax–van Leer (HLL) schemes [50,51] should be used without changing the properties of the physical time in order to explore fast computational speeds and reduce the stiffness for the low Mach number solar coronal region.

Furthermore, the time derivation preconditioning technique [52,53], is promising for solving the stiffness met in a solar wind simulation in the solar corona, where we have low speeds, i.e., low characteristic Mach numbers for sound, fast magnetosonic speed and Alfvénic speeds. However, proceeding in an MHD simulation including all speed situations like that used in fluid mechanics [50,51] is still challenging since more characteristic wave modes exist for MHD equations. These considerations will be left for our future work.

Acknowledgments

The work was jointly supported by the National Basic Research Program of China (Grant No. 2012CB825601), the National Natural Science Foundation of China (Grant Nos. 41231068, 41031066, 41274192, 41204127 & 41174150), the Knowledge Innovation Program of the Chinese Academy of Sciences (Grant No. KZZD-EW-01-4), and the Specialized Research Fund for State Key Laboratories. The numerical calculation has been completed on our SIGMA Cluster computing system. We are appreciated for our reviewers' comments and suggestions in the improvement of this paper.

References

[1] Wu ST, Dryer M. Comparative analyses of current three-dimensional numerical solar wind models. Sci China: Earth Sci 2015;58. http://dx.doi.org/10.1007/s11430-015-5062-1.
[2] Kifonidis K, Müller E. On multigrid solution of the implicit equations of hydrodynamics: experiments for the compressible Euler equations in general coordinates. Astron Astrophys 2012;544:A47.
[3] Feng XS, Xiang CQ, Zhong DK. GPU-accelerated computing of three-dimensional solar wind background. Sci China: Earth Sci 2013;56:1864–80.
[4] Berger MJ, Colella P. Local adaptive mesh refinement for shock hydrodynamics. J Comput Phys 1989;82:64–84.
[5] Tóth G, van der Holst B, Sokolov IV, de Zeeuw DL, Gombosi TI, Fang F, et al. Adaptive numerical algorithms in space weather modeling. J Comput Phys 2012;231:870–903.
[6] Feng XS, Zhang SH, Xiang CQ, Yang LP, Jiang CW, Wu ST. A hybrid solar wind model of the CESE+HLL method with a Yin-Yang overset grid and an AMR grid. Astrophys J 2011;734:50.
[7] Feng XS, Yang LP, Xiang CQ, Jiang CW, Ma XP, Wu ST, et al. Validation of the 3D AMR SIP-CESE solar wind model for four Carrington rotations. Solar Phys 2012;279:207–29.
[8] Rossow CC. Efficient computation of compressible and incompressible flows. J Comput Phys 2007;220:879–99.
[9] Jardin SC. Review of implicit methods for the magnetohydrodynamic description of magnetically confined plasmas. J Comput Phys 2012;231:822–38.
[10] Jones OS, Shumlak U, Eberhardt DS. An implicit scheme for nonideal magnetohydrodynamics. J Comput Phys 1997;130:231–42.
[11] Balci S, Aslan N. Two-dimensional MHD solver by fluctuation splitting and dual time stepping. Int J Numer Methods Fluids 2007;53:1585–611.
[12] Li D, Merkle C, Scott WM, Keefer D, Moeller T, Rhodes R. Hyperbolic algorithm for coupled plasma/electromagnetic fields including conduction and displacement currents. AIAA J 2011;49:909–20.
[13] Thompson J, Wilsony A, Moeller T. An AUSM-based algorithm for solving the coupled Navier–Stokes and Maxwell equations. AIAA 2013-3005; 2013.
[14] Thompson RJ, Wilson A, Moeller T, Merkle CL. A strong conservative Riemann solver for the solution of the coupled Maxwell and Navier–Stokes equations. J Comput Phys 2014;258:431–50.
[15] Sitaraman H, Raja LL. A matrix free implicit scheme for solution of resistive magneto-hydrodynamics equations on unstructured grids. J Comput Phys 2013;251:364–82.
[16] Tanaka T. Finite volume TVD scheme on an unstructured grid system for three-dimensional MHD simulation of inhomogeneous systems including strong background potential fields. J Comput Phys 1994;111:381–90.
[17] Feng XS, Yang LP, Xiang CQ, Wu ST, Zhou YF, Zhong DK. Three-dimensional solar wind modeling from the Sun to Earth by a SIP-CESE MHD model with a six-component grid. Astrophys J 2010;723:300–19.
[18] Ziegler U. A central-constrained transport scheme for ideal magnetohydrodynamics. J Comput Phys 2004;196:393–416.
[19] Fuchs FG, Mishra S, Risebro NH. Splitting based finite volume schemes for ideal MHD equations. J Comput Phys 2009;228:641–60.
[20] Ziegler U. A semi-discrete central scheme for magnetohydrodynamics on orthogonal-curvilinear grids. J Comput Phys 2011;230:1035–63.
[21] Arge CN, Odstrcil D, Pizzo VJ, Mayer LR. Improved method for specifying solar wind speed near the sun. In: Solar wind ten. The American Institute of Physics conference series, vol. 679; 2003. p. 190–3.
[22] Arge CN, Luhmann JG, Odstrcil D, Schrijver CJ, Li Y. Stream structure and coronal sources of the solar wind during the May 12th, 1997 CME. J Atmos Solar Terr Phys 2004;66:1295–309.
[23] Owens MJ, Arge CN, Spence HE, Pembroke A. An event-based approach to validating solar wind speed predictions: high-speed enhancements in the Wang–Sheeley–Arge model. J Geophys Res 2005;110:A12105.
[24] Feng XS, Zhang M, Zhou YF. A new three-dimensional solar wind model in spherical coordinates with a six-component grid. Astrophys J Suppl Ser 2014;214:6.
[25] Kley W. On the treatment of the coriolis force in computational astrophysics. Astron Astrophys 1998;338:L37–41.
[26] Feng XS, Xiang CQ, Zhong DK, Zhou YF, Yang LP, Ma XP. SIP-CESE MHD model of solar wind with adaptive mesh refinement of hexahedral meshes. Comput Phys Commun 2014;185:1965–80.
[27] Parker EN. Interplanetary dynamical processes. New York: Interscience Publishers; 1963.
[28] Jameson A. Time dependent calculations using multigrid, with applications to unsteady flows past airfoils and wings. AIAA Paper 91-1596; 1991.
[29] Yuan L. Comparison of implicit multigrid schemes for three-dimensional incompressible flows. J Comput Phys 2002;177:134–55.
[30] Chen X, Zha GC. Implicit application of non-reflective boundary conditions for Navier–Stokes equations in generalized coordinates. Int J Numer Methods Fluids 2006;50:767–93.
[31] Housman JA, Barad MF, Kiris CC, Kwak D. Space-time convergence analysis of a dual-time stepping method for simulating ignition overpressure waves. In: Computational fluid dynamics 2010. Springer; 2011. p. 45–652.
[32] Hundhausen AJ. Coronal expansion and solar wind. New York: Springer; 1972.
[33] Pneuman GW, Kopp RA. Gas-magnetic field interactions in the solar corona. Solar Phys 1971;18:258–70.
[34] Zhao XP, Hoeksema JT. The magnetic field at the inner boundary of the heliosphere around solar minimum. Solar Phys 2010;266:379–90.
[35] Wang YM, Sheeley NR, Howard RA, Cyr OCS, Simnett GM. Coronagraph observations of inflows during high solar activity. Geophys Res Lett 1999;26:1203–6.
[36] Sheeley NRJ, Warren HP, Wang YM. The origin of postflare loops. Astrophys J 2004;616:1224.
[37] Schwadron NA, Connick DE, Smith C. Magnetic flux balance in the heliosphere. Astrophys J Lett 2010;722:L132.
[38] Smith CW, Schwadron NA, DeForest CE. Decline and recovery of the interplanetary magnetic field during the protracted solar minimum. Astrophys J 2013;775:59.
[39] Zhao XP, Hoeksema JT. Prediction of the interplanetary magnetic field strength. J Geophys Res 1995;100:19–33.
[40] Zhao XP, Hoeksema JT, Rich NB. Modeling the radial variation of coronal streamer belts during sunspot ascending phase. Adv Space Res 2002;29:411–6.
[41] Odstrcil D, Riley P, Zhao XP. Numerical simulation of the 12 may 1997 interplanetary CME event. J Geophys Res 2004;109:A02116.
[42] Hayashi K. Magnetohydrodynamic simulations of the solar corona and solar wind using a boundary treatment to limit solar wind mass flux. Astrophys J Suppl Ser 2005;161:480–94.
[43] Hayashi K, Benevolenskaya E, Hoeksema T, Liu Y, Zhao XP. Three-dimensional magnetohydrodynamic simulation of a global solar corona using a temperature distribution map obtained from SOHO EIT measurements. Astrophys J 2006;636:L165.
[44] Powell KG, Roe PL, Linde TJ, Gombosi TI, De Zeeuw DL. A solution-adaptive upwind scheme for ideal magnetohydrodynamics. J Comput Phys 1999;154:284–309.
[45] Reynolds DR, Samtaney R, Woodward CS. A fully implicit numerical method for single-fluid resistive magnetohydrodynamics. J Comput Phys 2006;219:144–62.
[46] Adamsa MF, Samtaney R, Brandt A. Toward textbook multigrid efficiency for fully implicit resistive magnetohydrodynamics. J Comput Phys 2010;229:6208–19.
[47] Samtaney R, Adams M, Colella P, Graves D, Ligocki T, van Straalen B. An all-speed projection method for magneto-hydrodynamics. In: APS division of fluid dynamics meeting abstracts; 2010. p. 2.
[48] Samtaney R. Implicit numerical methods for magnetohydrodynamics. In: Topics in magnetohydrodynamics. Shanghai, China; 2012. p. 59–84.
[49] Reynolds DR, Samtaney R, Tiedeman HC. A fully implicit Newton–Krylov–Schwarz method for tokamak magnetohydrodynamics: Jacobian construction and preconditioner formulation. Comput Sci Discov 2012;5:014003.
[50] Park SH, Lee JE, Kwon JH. Preconditioned HLLE method for flows at all mach numbers. AIAA J 2006;44:2645–53.
[51] Li XS, Gu CW. Mechanism of roe-type schemes for all-speed flows and its application. Comput Fluids 2013;86:56–70.
[52] Turkel E. Preconditioning techniques in computational fluid dynamics. Annu Rev Fluid Mech 1999;31:385–416.
[53] Pandya SA, Venkateswaran S, Pulliam TH. Implementation of preconditioned dual-time procedures in overflow. AIAA 2003-0072; 2003.